

Quasi-10-day wave and semi-diurnal tide nonlinear interactions during the southern hemispheric SSW 2019 observed in the northern hemispheric mesosphere

Maosheng He¹, Jorge L. Chau¹, Jeffrey M Forbes², Denise Thorsen³, Guozhu Li⁴, Tarique A Siddiqui¹, Yosuke Yamazaki⁵, and Wayne K. Hocking⁶

¹Leibniz-Institute of Atmospheric Physics at the Rostock University

²University of Colorado Boulder

³University of Alaska Fairbanks

⁴Institute of Geology and Geophysics, Chinese Academy of Sciences

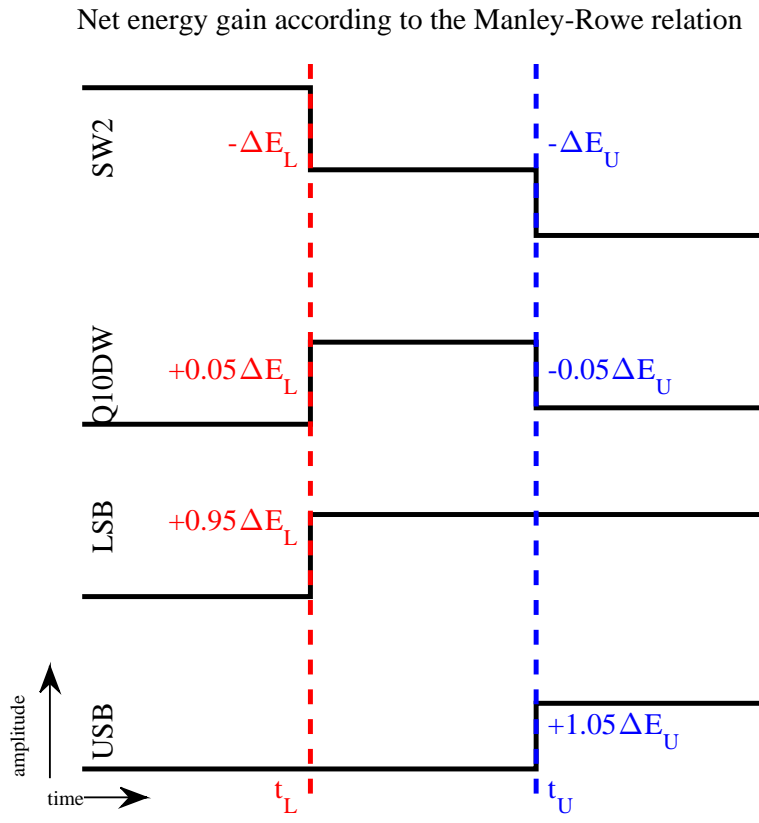
⁵GFZ German Research Centre for Geosciences

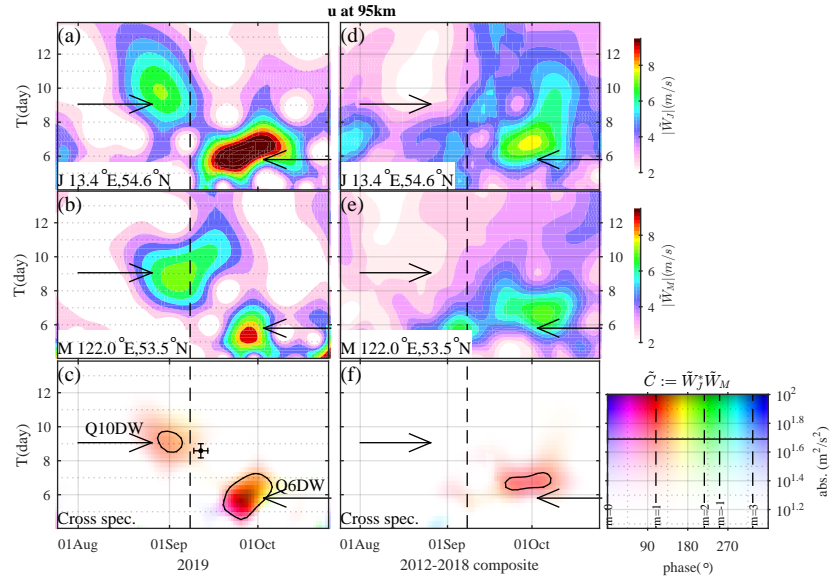
⁶University of Western Ontario

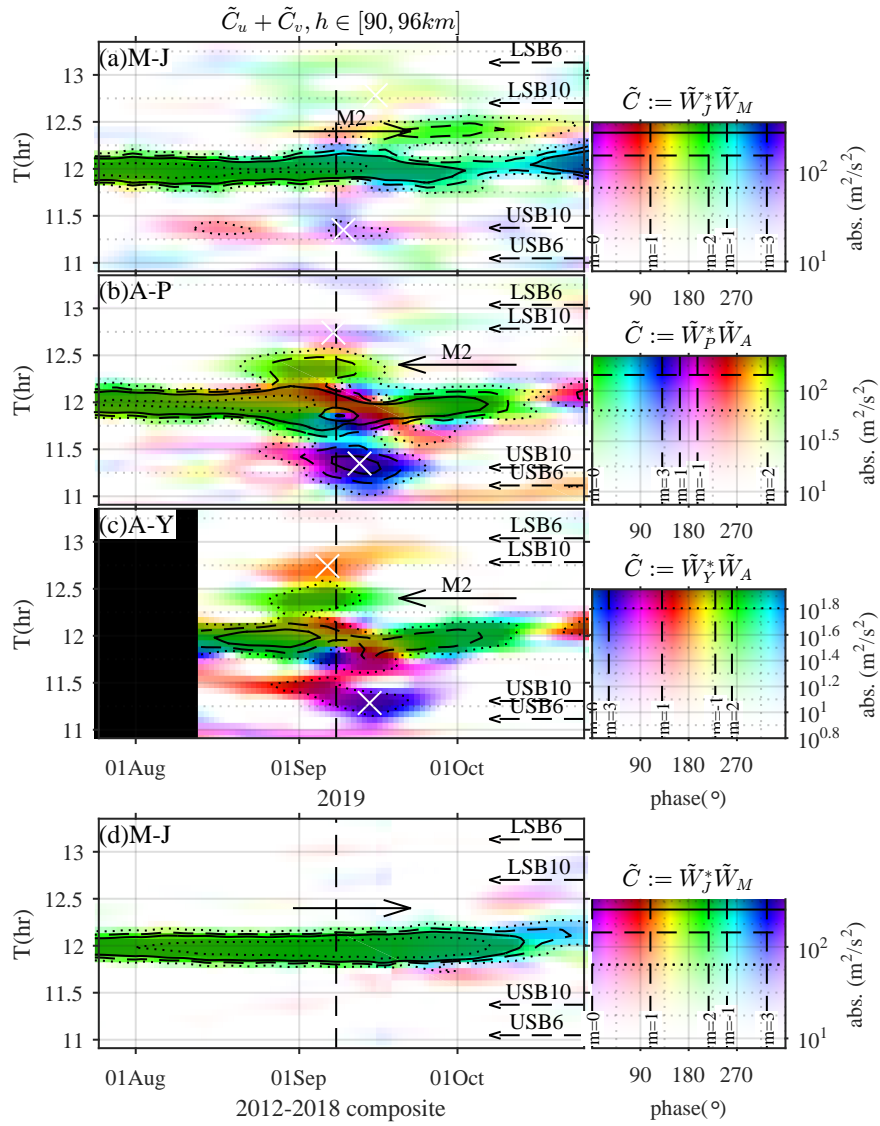
November 22, 2022

Abstract

Mesospheric winds from three longitudinal sectors at about 65°N and 54°N latitude are combined to diagnose the zonal wavenumbers (m) of high-frequency-resolved spectral wave signatures during the rare southern hemisphere sudden stratospheric warming (SSW) of 2019. Diagnosed are quasi-10- and 6-day planetary waves (Q10DW and Q6DW, $m=1$), solar semi-diurnal tides with $m=1, 2, 3$ (SW1, SW2, and SW3), lunar semi-diurnal tide, and the upper and lower sidebands (USB and LSB, $m=1$ and 3) of Q10DW-SW2 nonlinear interaction. We further present a 7-year composite analysis to distinguish SSW effects from climatological behaviors. Immediately before (after) the SSW onset, LSB (USB) enhances, accompanied by the enhancing (fading) Q10DW, and a weakening of climatological SW2 maximum. These behaviors are explained in terms of Manley-Rowe energy relation, i.e., the energy goes first from SW2 to Q10DW and LSB, and then from SW2 and Q10DW to USB.







Abstract

Mesospheric winds from three longitudinal sectors at about 65°N and 54°N latitude are combined to diagnose the zonal wavenumbers (m) of high-frequency-resolved spectral wave signatures during the rare southern hemisphere sudden stratospheric warming (SSW) of 2019. Diagnosed are quasi-10- and 6-day planetary waves (Q10DW and Q6DW, $m=1$), solar semi-diurnal tides with $m=1, 2, 3$ (SW1, SW2, and SW3), lunar semi-diurnal tide, and the upper and lower sidebands (USB and LSB, $m=1$ and 3) of Q10DW-SW2 non-linear interaction. We further present a 7-year composite analysis to distinguish SSW effects from climatological behaviors. Immediately before (after) the SSW onset, LSB (USB) enhances, accompanied by the enhancing (fading) Q10DW, and a weakening of climatological SW2 maximum. These behaviors are explained in terms of Manley-Rowe energy relation, i.e., the energy goes first from SW2 to Q10DW and LSB, and then from SW2 and Q10DW to USB.

Plain Language Summary

Sudden stratospheric warming events occur typically over the winter Arctic and are well-known for being accompanied by diverse waves. A rare SSW occurred in the southern hemisphere in September 2019. Here, we combine mesospheric observations from the northern hemisphere to study the wave activities before and during the warming event. A dual-station approach is implemented on high-frequency-resolved spectral peaks to diagnose the horizontal scales of the dominant waves. Diagnosed are multiple tidal components, multiple Rossby normal modes, and two secondary waves arising from non-linear interactions between a tide component and a Rossby wave. Most of these waves do not occur in a climatological sense and occur around the warming onset. Furthermore, the evolution of these waves can be explained using theoretical energy arguments.

1 Introduction

In the winter polar atmosphere, upward propagating Rossby waves (RWs, also called planetary waves), e.g., triggered by topography and the horizontal thermal gradient of the land-sea distribution. Such interactions may interact with the polar vortex and heat the stratosphere rapidly, known as sudden stratospheric warming events (SSWs, e.g., Butler et al., 2015). Associated with SSWs are oscillations in the middle and upper atmosphere in both neutral and plasma properties, such as the neutral density and composition, temperature, wind, plasma density, and electric current density (e.g., Chau et al., 2009; Goncharenko & Zhang, 2008; Pedatella & Forbes, 2010; He & Chau, 2019).

In the mesosphere, planetary-scale oscillations during SSWs can be categorized into two temporal scales, longer and shorter than one day, termed hereafter as RW- and tide-like oscillations, respectively. RW-like oscillations occur at periods from a few days to a few tens of days, mostly explained as RW normal modes (RNMs, e.g., Madden, 1979; Forbes, 1995). RNMs are westward-propagating and occur with wave periods near 2, 6, 10, 16, and days, and are often referred to as quasi-2-, 6-, 10-, 16-, and 28-day waves (Q2DW, Q6DW, Q10DW, Q16DW, and Q28DW, e.g., Forbes et al., 2017, 2020; Yamazaki, 2018; Zhao et al., 2019). Associations between RNMs and SSWs have also been broadly reported, although the underlying mechanisms are still under debate (e.g., He, Yamazaki, et al., 2020; Pancheva et al., 2008; Stray et al., 2015; Yamazaki & Matthias, 2019). Besides RNMs, secondary waves of nonlinear interactions between RNMs and stationary RWs are also observed during SSWs (e.g., He, Yamazaki, et al., 2020).

Oscillations, occurring around the periods of harmonics of the solar or lunar day, are explained mostly as signatures of harmonics of solar or lunar tides. Oscillations of this nature are reported to be associated with or impacted by SSWs, such as the first six solar migrating tidal harmonics (at 24hr, 12hr, ..., 4hr) and the second lunar migrating tidal harmonic (M2, at 12.4hr) (e.g., He, Forbes, et al., 2020; Chau et al., 2015; He & Chau, 2019). Among these oscillations, the sun-synchronous (migrating tide-like) components are typically explained in terms of SSW modulations of tidal heating (e.g., Goncharenko et al., 2012; Limpasuvan et al., 2016; Siddiqui et al., 2020) and of propagation conditions (e.g., He, Forbes, et al., 2020), whereas the non-sun-synchronous (non-migrating tide-like) components are conventionally explained as arising from zonal asymmetries in heating, or nonlinear interactions between stationary RWs and migrating tides (e.g., He et al., 2017; Forbes et al., 2020). Nonlinear interactions could also occur between RNMs

79 and tides (e.g., Forbes et al., 2020; He et al., 2017), generating secondary waves at fre-
80 quencies slightly below and above the tidal frequencies, termed hereafter as lower and
81 upper sidebands (LSBs and USBs), respectively. LSBs and USBs are often misinterpreted
82 as tides according to He and Chau (2019).

83 Most knowledge of the above mesospheric wave activities is based on SSWs that
84 occurred in the northern hemisphere (NH). In September 2019, an SSW occurred (Lim
85 et al., 2020) in the southern hemisphere (SH), providing a unique opportunity to inves-
86 tigate the response of the NH middle and upper atmosphere to SH SSWs. Using Aura
87 Microwave Limb Sounder (MLS) observations and Swarm plasma and magnetic obser-
88 vations, Yamazaki et al. (2020) revealed 6-day periodicities in the middle atmosphere
89 and ionosphere. Conventionally, such like periodicities were explained most often as Q6DW.
90 However, a recent modeling study (Miyoshi & Yamazaki, 2020) suggested that the iono-
91 spheric 6-day periodicities in the 2019 case might not be Q6DW signatures but aliases
92 from near-12hr waves resulted from Q6DW-SW2 nonlinear interaction. This aliasing, be-
93 tween RNWs and their secondary waves associated with migrating tides, is an inherent
94 sampling property of all quasi-sun-synchronous single-spacecraft missions, which is ex-
95 plained mathematically in Appendix A. The current work uses ground-based observa-
96 tions to eliminate the concerns about the aliasing and investigate the potential RNMs
97 and near-12hr waves. Implementing a dual-station approach, we are also able to diag-
98 nose zonal wavenumbers of the underlying waves, beyond the capabilities of single-station
99 approaches. Our results illustrate the presence of both RNMs and near-12h waves in the
100 mesosphere, and reveal how the Q10DW-tidal interactions result in the mesospheric wind
101 variability during the SH SSW.

102 **2 Observation and method**

103 The current work uses five radar systems, at Juliusruh (13.4°E, 54.6°N), Mohe (122°E,
104 53.5°N), Andenes(16.0°E, 69.3°N), PokerFlat (147.5°W,65.1°N), and Yellowknife (114.3°W,
105 62.5°N), referred hereafter as J, M, A, P and Y radars, respectively. The details of the
106 radar setups, e.g., frequencies and antenna configurations, were introduced in Hoffmann
107 et al. (2010); Yu et al. (2013); Singer et al. (2013); Klemm (2019); Kumar and Hocking
108 (2010), respectively. As illustrated by two dashed lines in Figure S1 in Supporting in-
109 formation (SI), these radars distribute largely along two latitudes, 65°N and 54°N. The
110 zonal and meridional wind observations (u and v) around the SSW, between 1 June and

111 31 November 2019 (except at Yellowknife where data is not available before 13 August),
 112 are derived between 80km and 100km altitude for a case study. As a reference and for
 113 comparison, 7-year (2012-2018) observations at Mohe and Juliusruh are also used for a
 114 composite analysis (CA).

115 Our main approach is the so-called phase differencing technique (PDT), developed
 116 in He, Chau, Stober, et al. (2018) and has been explained mathematically and imple-
 117 mented several times (e.g., He, Chau, Hall, et al., 2018). Here, we explain PDT briefly.
 118 Based on dual-point configurations, PDT makes use of the phase difference between two
 119 locations on the wave path to estimate the wavenumber in the direction defined by the
 120 two points (The same idea was also used in, e.g., the deconvolution procedure Hocking
 121 et al., 2014). When the two locations are at the same latitude, estimated would be the
 122 zonal wavenumber m . The estimation is based on two main assumptions. The first one,
 123 called single wave assumption, is that the wavenumber is a function of frequency. The
 124 other, called long wave assumption, is that the separation between the two locations is
 125 shorter than half the wavelength of the underlying wave. Particularly, in diagnosing RWs
 126 and tides, m could be assumed as a near-zero integral number, which might relax the
 127 long wave assumption from half wavelength to one and a half wavelength. PDT has been
 128 implemented, through cross-wavelet (CWL) analysis, to diagnose m of RW- and tide-
 129 like oscillations in a few NH SSWs (e.g., He, Chau, Stober, et al., 2018; He, Yamazaki,
 130 et al., 2020). Further validating PDT, different dual-station configurations at the same
 131 latitude yielded consistent results (e.g., He, Forbes, et al., 2020). The current work ap-
 132 plies PDT to the SH SSW 2019, using three dual-radar configurations, i.e., M-J, P-A,
 133 and Y-A.

134 **3 Results**

135 As explained in the introduction, most planetary-scale wave activities during SSWs
 136 are RW- and tide-like oscillations. Therefore, we explore the waves in two frequency ranges
 137 in Sections 3.1 and 3.2, respectively. Section 3.3 focuses only on $T = 12.0 \pm 0.2$ hr.

138 **3.1 Multi-day oscillations**

139 Figure 1a presents $|\tilde{W}_{(f,t)}^J|$, a Gabor wavelet (Torrence & Compo, 1998) of the zonal
 140 wind at 95km altitude over Juliusruh. In the plot, the dashed vertical line on 08 Septem-
 141 ber denotes the onset of the SH SSW 2019. The onset refers to the central day between

142 5-11 September, during which the atmospheric temperature at 10 hPa increased rapidly
 143 from 208K to 259K according to the MERRA2 reanalysis data (e.g., Yamazaki et al.,
 144 2020). The most dominant character of Figure 1a is the peak at periods $T= 6-8$ days
 145 around 1 October, as highlighted by a horizontal arrow. There is another peak around
 146 $T= 10$ days around 1 September, before the onset and highlighted by an arrow. Both
 147 of the 6- and 10-day peaks also occurred over Mohe, as displayed in the spectrum $|\tilde{W}_{(f,t)}^M|$
 148 in Figure 1b. The coincidence between the two radars allows diagnosis of m through CWL
 149 analysis (readers are referred to, e.g., He, Yamazaki, et al., 2020, for details), The CWL
 150 spectrum between Figures 1a and 1b, $\tilde{C}_{(f,t)} = \tilde{W}_{(f,t)}^{J*} \tilde{W}_{(f,t)}^M$, is shown in Figure 1c, in
 151 which the darkness denotes the amplitude $|\tilde{C}|$ while the color hue denotes $Arg\{\tilde{C}\}$. $Arg\{\tilde{C}\}$
 152 measures the phase difference of the oscillations between the stations. Assuming the phase
 153 difference is due to the propagation of a dominant wave with the wavenumber m , then
 154 $Arg\{\tilde{C}\} = m\lambda_{\Delta}$ is a function of m and the longitudinal separation between the two
 155 radars λ_{Δ} . The color hue of Figure 1c is adjusted so that the redness represents $Arg\{\tilde{C}\} =$
 156 λ_{Δ} , corresponding to $m=1$. In Figure 1c, both the 6- and 10-day peaks are associated
 157 with $m=1$, suggesting both peaks are the RNMs, i.e., Q6DW and Q10DW, respectively.
 158 Similar Q6DW and Q10DW signatures occur also at 65°N detected by the P-A radar
 159 pair, as displayed in Figure S2d in SI.

160 For comparison and as a reference, we present a CA in Figures 1d-f, using the data
 161 from J-M pair between 2012 and 2018. Similarly to the 2019 case, in Figures 1d-f Q6DW
 162 also occurs around 1 October, whereas Q10DW is not visible around 1 September which
 163 is different from the 2019 case.

164 3.2 Near-12hr oscillations

165 Figure 2a presents a CWL spectrum similar to Figure 1c but for the altitude-averaged
 166 spectrum at periods near 12hr. Different from Figure 1c showing the spectrum of only
 167 u , Figure 2a displays the sum of the spectra of u and v since the spectra are almost iden-
 168 tical to each other. The black isolines denote amplitudes at $\sqrt{|\tilde{C}|} = 8, 12, 16,$ and 24m/s .
 169 In Figure 2a, the most dominant peak occurs at 12.0hr, characterized by $m=2$ and $\sqrt{|\tilde{C}|} >$
 170 24m/s before the SSW onset, corresponding to the tidal component SW2. In the cur-
 171 rent work, SW m denotes semi-diurnal westward propagating component with zonal wavenum-
 172 ber m . In Figure 2a and at 12.4hr, as indicated by a horizontal arrow, another peak oc-

173 curs above $\sqrt{|\tilde{C}|} > 12\text{m/s}$. The 12.4hr peak is characterized by $m=2$, and therefore should
 174 be a signature of the lunar tide M2.

175 Figure 2b is the same plot as Figure 2a but from the radar pair A-P, at 65°N . Sim-
 176 ilarly to Figure 2a, in Figure 2b the spectrum also maximizes at 12.0hr and 12.4hr above
 177 $\sqrt{|\tilde{C}|} > 24\text{m/s}$ and 12m/s , respectively. The 12.0hr peak is mostly characterized by $m=2$,
 178 and so is the 12.4hr peak, which therefore suggests the underlying waves are SW2 and
 179 M2, respectively. In addition, in Figure 2b and between 11.0-11.5hr, there is a dominant
 180 blue peak, maximizing at $\sqrt{|\tilde{C}|} = 17.9\text{m/s}$, at $T = 11.36\text{hr}$ on 12 September 2019, as in-
 181 dicated by the white cross. However, the color of the 11.36hr is close to $m=1$ and $=3$
 182 in the color code map, due to the special radar separation $\lambda_\Delta \approx \pi$ and $\lambda_\Delta + 2\pi \approx 3\lambda_\Delta$.
 183 To determine m , we produce the same spectra as Figure 2b but for the radar pair A-Y,
 184 displayed in Figure 2c.

185 Similarly to Figure 2b, Figure 2c also exhibits peaks at $T = 12.4\text{hr}$, 12.0hr and 11.0 -
 186 11.5hr . The previous two are associated with $m=2$, whereas the third peak, as illustrated
 187 by the white cross, maximizes at $\sqrt{|\tilde{C}|} = 11.1\text{m/s}$, at $T = 11.29\text{hr}$ on 14 September 2019.
 188 The blueness suggests the underlying dominant wave is associated with $m=3$, which is
 189 compatible with the blue peak in Figures 2b. Actually, the color codes for all panels of
 190 Figure 2 are adapted so that the blueness represents $m=3$. A weak blue or purple peak
 191 could also be found in Figure 2a as indicated by the white cross, maximizing at $\sqrt{|\tilde{C}|} = 9.1\text{m/s}$,
 192 $T = 11.36\text{hr}$. Additionally, in Figure 2c and immediately before the onset, a red peak oc-
 193 curs at $T = 12.73\text{hr}$ with $\sqrt{|\tilde{C}|} = 8.0\text{m/s}$ as indicated by a white cross. The redness sug-
 194 gests the underlying wave is associated with $m=1$. Similar 12.7hr peaks also occur in Fig-
 195 ures 2b and 2a, indicated by white crosses there.

196 Figure 2d displays the same plot as Figure 2a but from the 7-year CA, which com-
 197 prises mainly the 12.0hr peak but not the off-12.0hr peaks seen in Figures 2a-c, at least
 198 not at the comparable magnitudes. The 12.0hr peak is also different from those in Fig-
 199 ures 2a-c, e.g., the peak exhibits a minimum in late October in Figure 2d, but prema-
 200 turely around 1 October in Figure 2a. We look into the details in the next subsection.

201 3.3 Solar semi-diurnal tide

202 To investigate the 12.0hr peak, we reproduce spectra similar to Figure 2a but at
 203 every individual altitude, and then pick the values only at $T = 12.0 \pm 0.2\text{hr}$ at each alti-
 204 tude and combine them into the time-height plane, displayed in Figure 3a. Similarly, Fig-

205 ures 3b, 3c, and 3d are constructed from spectra similar to Figures 2b, 2c, and 2d. In
 206 all panels here, green represents $m=2$. The most dominant character in Figure 3d is the
 207 green peak ($m=2$), maximizing vertically at about 90km in September. The September
 208 maximum is a well-known climatological behavior (also cf., Figures 7b and 1c in He &
 209 Chau, 2019; Conte et al., 2017, respectively). The pattern around the SSW in Figure 3a
 210 could be explained as a distorted version of the climatological maximum. The maximum
 211 occurs 10-20d earlier and splits around 90km and above, in comparison with Figure 3d.

212 The premature and split maximum also occurs in Figures 3b and 3c, but associ-
 213 ated with more interesting behaviors. As indicated by the horizontal arrows, blueness
 214 (or purpleness) and redness occur at $h=90$ km and 95km, respectively. These colors sug-
 215 gest that the dominant underlying wave there is not SW2. In Figure 3c, blueness and
 216 redness represent $m=1$ and 3, suggesting the underlying waves are the non-migrating
 217 tides, SW1 and SW3, respectively.

218 4 Discussions

219 The previous section diagnoses the zonal wavenumber m of potential waves seen
 220 in cross wavelet spectra, in two ranges of period, namely, multi-days and near-12hr. In
 221 the current section, we discuss them as RNMs, tides, and secondary waves of RNM-tide
 222 nonlinear interactions.

223 4.1 Association of RNMs with SH SSW

224 Although there are observational studies suggesting that SSWs are not associated
 225 with RNMs (e.g., Sassi et al., 2012), most observational studies support associations, at
 226 least for most NH SSWs between 2004 and 2018 (e.g., He, Yamazaki, et al., 2020; Pancheva
 227 et al., 2008; Stray et al., 2015; Yamazaki & Matthias, 2019; Gong et al., 2018; Yamazaki,
 228 2018; Chandran et al., 2013; Manney et al., 2008). The burst of Q6DW in late Septem-
 229 ber 2019 was reported by Yamazaki et al. (2020) using geopotential height (GPH) ob-
 230 servations of Aura MLS and magnetic observations from Swarm. The 2019 Q6DW am-
 231 plitude, in GPH, was stronger than the 2004-2018 average amplitude, especially above
 232 70km altitude in SH. Consistently, our comparison between Figures 1c and 1f also illus-
 233 trates that in NH the 2019 Q6DW is also stronger than the multi-year average. How-
 234 ever, such a strong NH Q6DW in this season is not unique for 2019. Among the seven
 235 years we explored, Q6DW also occurred at comparable or even stronger amplitudes in

236 the same season in 2013 and 2017 (observed from the same figures as Figures 1a-c but
 237 for 2012-2018, not shown here).

238 In contrast to the climatological occurrence of the Q6DW, the occurrence of the
 239 Q10DW in early September is unique for 2019, and also temporally more close to the
 240 SH SSW, c.f. Figures 1a-c vs. 1d-f. Therefore, we argue that the Q10DW is potentially
 241 associated with the SSW. Consistent with our Q10DW results, the SH GPH results (Figure
 242 3a in Yamazaki et al., 2020) also exhibited a spectral peak, not mentioned by the au-
 243 thors, at $T=10$ d around 1 September and weaker than the Q6DW amplitude by at least
 244 50%. The consistency of our NH ground-based results with the SH satellite-based results
 245 suggests that the Q6DW and Q10DW are both active on global scales, consistent with
 246 their interpretation as RNM. Coincidentally, a Q10DW signature was also reported in
 247 the ionosphere during the SH 2002 (Mo & Zhang, 2020).

248 RNMs prior to NH SSW onsets could be explained in terms of in situ instability
 249 (e.g., Siskind et al., 2010; Pancheva et al., 2008), whereas the RNMs which appeared af-
 250 ter the NH SSWs are believed to arise from different mechanisms, e.g., the zonal asym-
 251 metry of gravity wave breaking (e.g., Manney et al., 2008). Therefore, the Q10DW might
 252 be attributable to potential in situ instabilities. Supporting this hypothesis is the evo-
 253 lution of the meridional gradient of the quasi-geostrophic potential derived from the MLS
 254 GPH observations (Figures 3h-j in Yamazaki et al., 2020). The gradient is necessary for
 255 barotropic/baroclinic instability, even though the evolution and the instability were dis-
 256 cussed to explain the Q6DW. Another potential mechanism of the Q10DW generation
 257 is the planetary wave amplification by stimulated tidal decay (PASTIDE, He et al., 2017)
 258 as detailed in the following subsection.

259 **4.2 Secondary waves of Q10DW-SW2 nonlinear interactions**

260 In Sections 3.2 and 3.3, we explained the 12.0hr and 12.4hr spectral peaks as so-
 261 lar and lunar tides, respectively. In the current subsection, we discuss other near-12hr
 262 peaks as the upper and lower sidebands (USB and LSB) of nonlinear interactions between
 263 SW2 and RNM, respectively.

264 According to the resonance conditions of wave-wave nonlinear interaction (e.g., He
 265 et al., 2017), the frequency and wavenumber of USB (LSB) are equal to the sum (dif-
 266 ference) of their parent waves. Given that the RNMs, Q6DW, Q10DW, and Q16DW,
 267 are associated with $m=1$, all their USBs and LSBs of interactions with SW2 are asso-

268 ciated with $m=3$, and 1, respectively. Observational evidence with constraints of both
 269 f and m were reported for the sidebands of Q6DW and Q16DW using either ground-
 270 based or satellite observations (e.g., Forbes & Zhang, 2017; Forbes et al., 2020; He, Chau,
 271 Hall, et al., 2018; He, Chau, Stober, et al., 2018). As a reference, the theoretical peri-
 272 ods of the USBs and LSBs of RNMs, according to the periods indicated by the arrows
 273 in Figures 1c and S1d, are calculated and displayed as the dashed horizontal arrows at
 274 the most right-side in all panels of Figure 2. Further, using the periods at the six white
 275 crosses (indexed hereafter as $k = 1, 2, \dots, 6$) in Figures 2a-c, we calculate the theoret-
 276 ically required periods of the parent RNMs according to the resonance condition, result-
 277 ing in six values T_k . Assuming all the six peaks share one parent RNM and using the
 278 spectral amplitude $w_k := |\tilde{C}_k| / \langle |\tilde{C}_k| \rangle_k$ in Figure 2, we calculate the weight aver-
 279 age $\bar{T} := \langle T_k w_k \rangle_k = 8.6\text{d}$ with a deviation $\sigma(w_k(T_k - \bar{T})) = 0.4\text{d}$, displayed as a verti-
 280 cal error bar in Figures 1c and S1. The horizontal error bar represents the correspond-
 281 ing weight-averaged time and its deviation, $\bar{t} = 11.1 \pm 2.2\text{d}$ after 00:00, on 1 September.
 282 In Figures 1c and S1d, the Q10DW peaks, in comparison with the Q6DW, are closer to
 283 the black cross in both t and T , and \bar{T} overlaps the period of the Q10DW peak partially.
 284 Therefore, we argue that the Q10DW, rather than Q6DW, is more likely responsible to
 285 the sidebands, or at least contributes more.

286 Moreover, the temporal evolution of the Q10DW peak, together with those of the
 287 LSB, USB, and SW2, satisfies the energy requirements of Manley-Rowe relation (He et
 288 al., 2017). According to the Manley-Rowe relation, the LSB and USB are generated in
 289 two nonlinear interaction processes. In the LSB-generating interaction, the tide exports
 290 energy to both LSB and RNM, while in the USB-generating interaction, both RNM and
 291 tide contribute energy to USB. A potential circumstance occurring during the SH SSW
 292 2019 is sketched in Figure 4. LSB-generating interaction occurs at t_L before the onset,
 293 generating or amplifying LSB and Q10DW at the cost of energy from SW2. Then, the
 294 amplified Q10DW further interacts with SW2 at t_U around the onset, in which both Q10DW
 295 and SW2 transport energy to the USB. This circumstance could explain following de-
 296 tails of the wave evolutions around the onset in Figures 1-3, namely, (1) the Q10DW and
 297 LSB burst simultaneously before the onset; (2) the USB maximizes after the weaken-
 298 ing of Q10DW; and meanwhile (3) the bursts of both LSB and USB are accompanied
 299 with the split September SW2 maximum as described in Section 3.3. According to the
 300 Manley-Rowe relation, the absolute net energy gains of the waves are proportional to

301 their frequencies, and 100% and 95% of the energy of the LSB and USB are contributed
302 directly by SW2. Therefore, the energy deficits of SW2 could be responsible for the split-
303 ting of the SW2 maximum in Figures 3a-c.

304 On the other hand, Q6DW maximized in late September and is, therefore, less likely
305 responsible for the LSB generation that occurred about 20-30 days prior.

306 5 Summary

307 The current study explores planetary-scale wave activities in the NH during the
308 SH SSW 2019, using mesospheric winds detected with five meteor radar systems around
309 54°N and 65°N. We diagnose the zonal wavenumber m of wave signatures contained in
310 cross-wavelet spectra of the observations from multiple longitudinal sectors. Spectral peaks
311 are diagnosed at $T= 5-7\text{d}$, $8-10\text{d}$, 12.0hr , 12.4hr , $11.2-11.5\text{hr}$, and $12.6-12.8\text{hr}$, associated
312 dominantly with $m= 1, 1, 2, 2, 3$, and 1 , which are explained as Q6DW, Q10DW, SW2,
313 M2, and USB and LSB of Q10DW-SW2 nonlinear interaction, respectively. As a refer-
314 ence, a 7-year composite analysis is presented, illustrating that the SW2 pattern dur-
315 ing the SH SSW could be explained as a premature and split climatological September
316 maximum, and that the Q6DW during the SH SSW could be explained as an amplified
317 climatological phenomenon. The detected periods of the Q10DW, LSB and USB signa-
318 tures satisfy the resonance conditions of nonlinear interaction. In addition, the tempo-
319 ral variations of the Q10DW, LSB, USB and SW2, shortly before and after the SSW on-
320 set, could be explained in terms of the Manley-Rowe relation of nonlinear interactions.
321 Our results illustrate that the Q10DW-SW2 interactions can explain the details of the
322 mesospheric wind variabilities during the SH SSW 2019.

323 Acknowledgments

324 This work is supported by the Deutsche Forschungsgemeinschaft (DFG, German Research
325 Foundation) under SPP 1788 (DynamicEarth) projects CH1482/1-2 (DYNAMITE-2).
326 Jeffrey M. Forbes acknowledges support under NSF Award AGS-1630177 to the Univer-
327 sity of Colorado Boulder. Support for the Poker Flat Meteor Radar was provided by the
328 National Science Foundation under grant AGS-1651464. The data from Mohe is provided
329 by the Data Center for Geophysics (<http://wdc.geophys.ac.cn/>), National Earth System
330 Science Data Sharing Infrastructure at BNOSE(Beijing National Observatory of Space
331 Environment), IGGCAS (Institute of Geology and Geophysics, Chinese Academy of Sci-

ences). The post-processed data in this paper are available at the Harvard Dataverse through
<https://doi.org/10.7910/DVN/KL6QUL>.

References

- Butler, A. H., Seidel, D. J., Hardiman, S. C., Butchart, N., Birner, T., & Match, A. (2015). Defining sudden stratospheric warmings. *Bull. Am. Meteorol. Soc.*, *96*(11), 1913–1928. doi: 10.1175/BAMS-D-13-00173.1
- Chandran, A., Garcia, R. R., Collins, R. L., & Chang, L. C. (2013). Secondary planetary waves in the middle and upper atmosphere following the stratospheric sudden warming event of January 2012. *Geophys. Res. Lett.*, *40*(9), 1861–1867. doi: 10.1002/grl.50373
- Chau, J. L., Fejer, B. G., & Goncharenko, L. P. (2009, mar). Quiet variability of equatorial $e \times B$ drifts during a sudden stratospheric warming event. *Geophys. Res. Lett.*, *36*(5), 2–5. Retrieved from <http://doi.wiley.com/10.1029/2008GL036785> doi: 10.1029/2008GL036785
- Chau, J. L., Hoffmann, P., Pedatella, N. M., Matthias, V., & Stober, G. (2015, apr). Upper mesospheric lunar tides over middle and high latitudes during sudden stratospheric warming events. *J. Geophys. Res. Sp. Phys.*, *120*(4), 3084–3096. Retrieved from <http://doi.wiley.com/10.1002/2015JA020998> doi: 10.1002/2015JA020998
- Conte, J. F., Chau, J. L., Stober, G., Pedatella, N., Maute, A., Hoffmann, P., ... Murphy, D. J. (2017). Climatology of semidiurnal lunar and solar tides at middle and high latitudes: Interhemispheric comparison. *J. Geophys. Res. Sp. Phys.*, *122*(7), 7750–7760. Retrieved from <http://dx.doi.org/10.1002/2017JA024396><http://onlinelibrary.wiley.com/store/10.1002/2017JA024396/asset/jgra53687.pdf?v=1&t=jansn8up&s=72eb34b0c842fc65e21955e9b8b7bfd8028227ee> doi: 10.1002/2017JA024396
- Forbes, J. M. (1995). Tidal and planetary waves. *Geophys. Monogr. Ser.*, *87*, 67–87. Retrieved from <http://www.agu.org/books/gm/v087/GM087p0067/GM087p0067.shtml> doi: 10.1029/GM087p0067
- Forbes, J. M., & Zhang, X. (2017). The quasi-6 day wave and its interactions with solar tides. *J. Geophys. Res. Sp. Phys.*, *122*(4), 4764–4776. Retrieved from <http://doi.wiley.com/10.1002/2017JA023954> doi:

- 364 10.1002/2017JA023954
- 365 Forbes, J. M., Zhang, X., Hagan, M. E., England, S. L., Liu, G., & Gasperini, F.
366 (2017). On the Specification of Upward-Propagating Tides for ICON Science
367 Investigations. *Space Sci. Rev.*, *212*(1-2), 697–713. Retrieved from [http://](http://dx.doi.org/10.1007/s11214-017-0401-5)
368 dx.doi.org/10.1007/s11214-017-0401-5 doi: 10.1007/s11214-017-0401-5
- 369 Forbes, J. M., Zhang, X., & Maute, A. (2020). Planetary wave (PW) generation
370 in the thermosphere driven by the PWmodulated tidal spectrum. *J. Geophys.*
371 *Res. Sp. Phys.*, 1–19. doi: 10.1029/2019ja027704
- 372 Goncharenko, L. P., Coster, A. J., Plumb, R. A., & Domeisen, D. I. (2012). The
373 potential role of stratospheric ozone in the stratosphere-ionosphere cou-
374 pling during stratospheric warmings. *Geophys. Res. Lett.*, *39*(8), 1–5. doi:
375 10.1029/2012GL051261
- 376 Goncharenko, L. P., & Zhang, S. R. (2008). Ionospheric signatures of sudden strato-
377 spheric warming: Ion temperature at middle latitude. *Geophys. Res. Lett.*,
378 *35*(21), 4–7. doi: 10.1029/2008GL035684
- 379 Gong, Y., Ma, Z., Lv, X., Zhang, S., Zhou, Q., Aponte, N., & Sulzer, M. (2018, dec).
380 A Study on the Quarterdiurnal Tide in the Thermosphere at Arecibo During
381 the February 2016 Sudden Stratospheric Warming Event. *Geophys. Res. Lett.*,
382 *45*(23), 13,142–13,149. Retrieved from [https://onlinelibrary.wiley.com/](https://onlinelibrary.wiley.com/doi/abs/10.1029/2018GL080422)
383 [doi/abs/10.1029/2018GL080422](https://onlinelibrary.wiley.com/doi/abs/10.1029/2018GL080422) doi: 10.1029/2018GL080422
- 384 He, M., & Chau, J. L. (2019). Mesospheric semidiurnal tides and near-12 h waves
385 through jointly analyzing observations of five specular meteor radars from
386 three longitudinal sectors at boreal midlatitudes. *Atmos. Chem. Phys.*, *19*(9),
387 5993–6006. Retrieved from [https://www.atmos-chem-phys.net/19/5993/](https://www.atmos-chem-phys.net/19/5993/2019/acp-19-5993-2019.html)
388 [2019/acp-19-5993-2019.html](https://www.atmos-chem-phys.net/19/5993-2019.html)
- 389 He, M., Chau, J. L., Hall, C. M., Tsutsumi, M., Meek, C., & Hoffmann, P. (2018).
390 The 16-Day Planetary Wave Triggers the SW1-Tidal-Like Signatures During
391 2009 Sudden Stratospheric Warming. *Geophys. Res. Lett.*, *45*(22), 12,631–
392 12,638. Retrieved from <http://doi.wiley.com/10.1029/2018GL079798> doi:
393 10.1029/2018GL079798
- 394 He, M., Chau, J. L., Stober, G., Hall, C. M., Tsutsumi, M., & Hoffmann, P. (2017).
395 Application of Manley-Rowe Relation in Analyzing Nonlinear Interactions Be-
396 tween Planetary Waves and the Solar Semidiurnal Tide During 2009 Sudden

- 397 Stratospheric Warming Event. *J. Geophys. Res. Sp. Phys.*, *122*(10), 10,783–
 398 10,795. Retrieved from <http://dx.doi.org/10.1002/2017JA024630> doi:
 399 10.1002/2017JA024630
- 400 He, M., Chau, J. L., Stober, G., Li, G., Ning, B., & Hoffmann, P. (2018). Re-
 401 lations Between Semidiurnal Tidal Variants Through Diagnosing the
 402 Zonal Wavenumber Using a Phase Differencing Technique Based on Two
 403 Ground-Based Detectors. *J. Geophys. Res. Atmos.*, *123*(8), 4015–4026.
 404 Retrieved from <http://doi.wiley.com/10.1002/2018JD028400> doi:
 405 10.1002/2018JD028400
- 406 He, M., Forbes, J. M., Chau, J. L., Li, G., Wan, W., & Korotyshkin, D. V. (2020,
 407 mar). High-Order Solar Migrating Tides Quench at SSW Onsets. *Geo-
 408 phys. Res. Lett.*, *47*(6). Retrieved from [http://doi.wiley.com/10.1029/
 409 2019GL086778](http://doi.wiley.com/10.1029/2019GL086778) doi: 10.1029/2019GL086778
- 410 He, M., Yamazaki, Y., Hoffmann, P., Hall, C. M., Tsutsumi, M., Li, G., & Chau,
 411 J. L. (2020). Zonal wavenumber diagnosis of Rossby wave like oscillations
 412 using paired ground based radars. *J. Geophys. Res. Atmos.*. Retrieved from
 413 <https://doi.org/10.1029/2019JD031599> doi: 10.1029/2019jd031599
- 414 Hocking, W. K., Hocking, A., Hocking, D. G., & Garbanzo-Salas, M. (2014). Wind-
 415 profiler optimization using digital deconvolution procedures. *J. Atmos. Solar-
 416 Terrestrial Phys.*, *118*, 45–54. Retrieved from [http://dx.doi.org/10.1016/j
 417 .jastp.2013.08.025](http://dx.doi.org/10.1016/j.jastp.2013.08.025) doi: 10.1016/j.jastp.2013.08.025
- 418 Hoffmann, P., Becker, E., Singer, W., & Placke, M. (2010). Seasonal varia-
 419 tion of mesospheric waves at northern middle and high latitudes. *J. At-
 420 mos. Solar-Terrestrial Phys.*, *72*(14), 1068–1079. Retrieved from [http://
 421 www.sciencedirect.com/science/article/pii/S1364682610001987](http://www.sciencedirect.com/science/article/pii/S1364682610001987) doi:
 422 <https://doi.org/10.1016/j.jastp.2010.07.002>
- 423 Klemm, J. (2019). *Classification and signal processing of radio backscatter from me-
 424 teors* (Doctoral dissertation). Retrieved from [http://hdl.handle.net/11122/
 425 10901](http://hdl.handle.net/11122/10901)
- 426 Kumar, G. K., & Hocking, W. K. (2010). Climatology of northern polar latitude
 427 MLT dynamics: Mean winds and tides. *Ann. Geophys.*, *28*(10), 1859–1876.
 428 doi: 10.5194/angeo-28-1859-2010
- 429 Lim, E.-P., Hendon, H. H., Butler, A. H., Garreaud, R. D., Polichtchouk, I., Shep-

- 430 herd, T. G., ... Nakamura, H. (2020). The 2019 Antarctic sudden strato-
 431 spheric warming. *SPARC Newsl.*(54), 10–undefined.
- 432 Limpasuvan, V., Orsolini, Y. J., Chandran, A., Garcia, R. R., & Smith, A. K.
 433 (2016). On the composite response of the MLT to major sudden stratospheric
 434 warming events with elevated stratopause. *J. Geophys. Res. Atmos.*, *121*(9),
 435 4518–4537. Retrieved from [https://agupubs.onlinelibrary.wiley.com/](https://agupubs.onlinelibrary.wiley.com/doi/abs/10.1002/2015JD024401)
 436 [doi/abs/10.1002/2015JD024401](https://doi.org/10.1002/2015JD024401) doi: 10.1002/2015JD024401
- 437 Madden, R. A. (1979). Observations of large-scale traveling Rossby waves. *Rev. Geo-*
 438 *phys.*, *17*(8), 1935–1949. doi: 10.1029/RG017i008p01935
- 439 Manney, G. L., Krüger, K., Pawson, S., Minschwaner, K., Schwartz, M. J., Daffer,
 440 W. H., ... Waters, J. W. (2008). The evolution of the stratopause during the
 441 2006 major warming: Satellite data and assimilated meteorological analyses. *J.*
 442 *Geophys. Res. Atmos.*, *113*(11), 1–16. doi: 10.1029/2007JD09097
- 443 Miyoshi, Y., & Yamazaki, Y. (2020). Excitation mechanism of ionospheric 6-day
 444 oscillation during the 2019 September sudden stratospheric warming event.
 445 *Earth Sp. Sci. Open Arch.*, *57*. Retrieved from [https://doi.org/10.1002/](https://doi.org/10.1002/essoar.10503242.1)
 446 [essoar.10503242.1](https://doi.org/10.1002/essoar.10503242.1) doi: 10.1002/essoar.10503242.1
- 447 Mo, X., & Zhang, D. (2020). Quasi-10-d wave modulation of an equatorial ionization
 448 anomaly during the Southern Hemisphere stratospheric warming of 2002. *Ann.*
 449 *Geophys.*, *38*(1), 9–16. doi: 10.5194/angeo-38-9-2020
- 450 Pancheva, D., Mukhtarov, P., Mitchell, N. J., Merzlyakov, E., Smith, A. K., An-
 451 donov, B., ... Murayama, Y. (2008). Planetary waves in coupling the
 452 stratosphere and mesosphere during the major stratospheric warming in
 453 2003/2004. *J. Geophys. Res. Atmos.*, *113*(12), 1–22. Retrieved from
 454 <http://dx.doi.org/10.1029/2007JD009011> doi: 10.1029/2007JD009011
- 455 Pedatella, N. M., & Forbes, J. M. (2010, jun). Evidence for stratosphere sudden
 456 warming-ionosphere coupling due to vertically propagating tides. *Geophys.*
 457 *Res. Lett.*, *37*(11), n/a–n/a. Retrieved from [http://doi.wiley.com/10.1029/](http://doi.wiley.com/10.1029/2010GL043560)
 458 [2010GL043560](https://doi.org/10.1029/2010GL043560) doi: 10.1029/2010GL043560
- 459 Salby, M. L. (1982, nov). Sampling Theory for Asynoptic Satellite Observa-
 460 tions. Part I: Space-Time Spectra, Resolution, and Aliasing. *J. Atmos.*
 461 *Sci.*, *39*(11), 2577–2600. Retrieved from [https://doi.org/10.1175/](https://doi.org/10.1175/1520-0469(1982)039<3C2577:STFAS0>3E2.0.CO;2)
 462 [1520-0469\(1982\)039<3C2577:STFAS0>3E2.0.CO;2](https://doi.org/10.1175/1520-0469(1982)039<3C2577:STFAS0>3E2.0.CO;2) doi: 10.1175/

- 463 1520-0469(1982)039(2577:STFASO)2.0.CO;2
- 464 Sassi, F., Garcia, R. R., & Hoppel, K. W. (2012). Large-Scale Rossby Normal Modes
465 during Some Recent Northern Hemisphere Winters. *J. Atmos. Sci.*, *69*(3),
466 820–839. doi: 10.1175/jas-d-11-0103.1
- 467 Siddiqui, T. A., Maute, A., & Pedatella, N. M. (2020). On the Importance of
468 Interactive Ozone Chemistry in Earth-System Models for Studying Mesosphere-
469 Lower Thermosphere Tidal Changes during Sudden Stratospheric Warmings.
470 *J. Geophys. Res. Sp. Phys.*. Retrieved from [https://onlinelibrary.wiley](https://onlinelibrary.wiley.com/doi/abs/10.1029/2019JA027193)
471 [.com/doi/abs/10.1029/2019JA027193](https://onlinelibrary.wiley.com/doi/abs/10.1029/2019JA027193) doi: 10.1029/2019JA027193
- 472 Singer, W., Hoffmann, P., Kishore Kumar, G., Mitchell, N. J., & Matthias, V.
473 (2013). Atmospheric Coupling by Gravity Waves: Climatology of Grav-
474 ity Wave Activity, Mesospheric Turbulence and Their Relations to Solar
475 Activity. In F.-J. Lübken (Ed.), *Clim. weather sun-earth syst. highlights*
476 *from a prior. progr.* (pp. 409–427). Dordrecht: Springer Netherlands. Re-
477 trieved from [https://doi.org/10.1007/978-94-007-4348-9{_}22](https://doi.org/10.1007/978-94-007-4348-9_{_}22) doi:
478 10.1007/978-94-007-4348-9_22
- 479 Siskind, D. E., Eckermann, S. D., McCormack, J. P., Coy, L., Hoppel, K. W., &
480 Baker, N. L. (2010). Case studies of the mesospheric response to recent mi-
481 nor, major, and extended stratospheric warmings. *J. Geophys. Res. Atmos.*,
482 *115*(20), 1–16. doi: 10.1029/2010JD014114
- 483 Stray, N. H., Orsolini, Y. J., Espy, P. J., Limpasuvan, V., & Hibbins, R. E. (2015).
484 Observations of planetary waves in the mesosphere-lower thermosphere during
485 stratospheric warming events. *Atmos. Chem. Phys.*, *15*(9), 4997–5005. doi:
486 10.5194/acp-15-4997-2015
- 487 Torrence, C., & Compo, G. P. (1998). A Practical Guide to Wavelet Analysis. *Bull.*
488 *Am. Meteorol. Soc.*, *79*(1), 61–78. doi: 10.1175/1520-0477(1998)079(0061:
489 APTWA)2.0.CO;2
- 490 Yamazaki, Y. (2018). Quasi-6-Day Wave Effects on the Equatorial Ionization
491 Anomaly Over a Solar Cycle. *J. Geophys. Res. Sp. Phys.*, *123*(11), 9881–9892.
492 doi: 10.1029/2018JA026014
- 493 Yamazaki, Y., & Matthias, V. (2019). Large Amplitude Quasi-10-day Waves in the
494 Middle Atmosphere during Final Warmings. *J. Geophys. Res.*, 1–19. doi: 10
495 .1029/2019JD030634

- 496 Yamazaki, Y., Matthias, V., Miyoshi, Y., Stolle, C., Siddiqui, T., Kervalishvili, G.,
497 ... Alken, P. (2020). September 2019 Antarctic Sudden Stratospheric Warm-
498 ing: Quasi6Day Wave Burst and Ionospheric Effects. *Geophys. Res. Lett.*,
499 47(1), 1–12. doi: 10.1029/2019GL086577
- 500 Yu, Y., Wan, W., Ning, B., Liu, L., Wang, Z., Hu, L., & Ren, Z. (2013). Tidal
501 wind mapping from observations of a meteor radar chain in December 2011. *J.*
502 *Geophys. Res. Sp. Phys.*, 118(5), 2321–2332. Retrieved from [https://agupubs](https://agupubs.onlinelibrary.wiley.com/doi/abs/10.1029/2012JA017976)
503 [.onlinelibrary.wiley.com/doi/abs/10.1029/2012JA017976](https://agupubs.onlinelibrary.wiley.com/doi/abs/10.1029/2012JA017976) doi: 10.1029/
504 2012JA017976
- 505 Zhao, Y., Taylor, M. J., Pautet, P.-D., Moffat-Griffin, T., Hervig, M. E., Murphy,
506 D. J., ... Russell III, J. M. (2019). Investigating an Unusually Large 28-Day
507 Oscillation in Mesospheric Temperature Over Antarctica Using Ground-Based
508 and Satellite Measurements. *J. Geophys. Res. Atmos.*, 124(15), 8576–8593.
509 Retrieved from [https://agupubs.onlinelibrary.wiley.com/doi/abs/](https://agupubs.onlinelibrary.wiley.com/doi/abs/10.1029/2019JD030286)
510 [10.1029/2019JD030286](https://agupubs.onlinelibrary.wiley.com/doi/abs/10.1029/2019JD030286) doi: 10.1029/2019JD030286

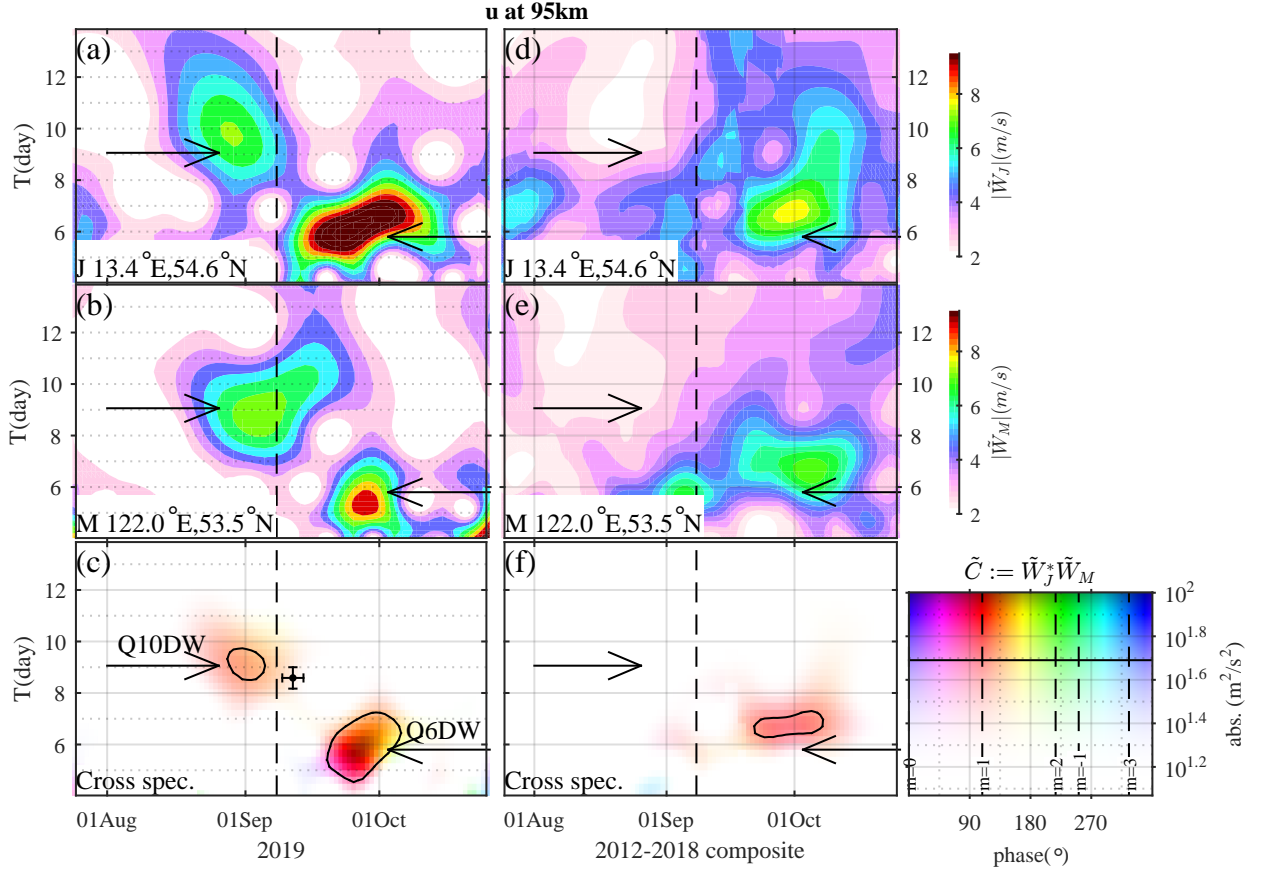


Figure 1: Wavelet spectra of the zonal wind at 95km altitude over the radar systems at (a) Juliusruh and (b) Mohe, and (c) their cross wavelet spectrum. In each Panel, the vertical dashed line represents the SH SSW onset; the horizontal arrows indicate the periods of the maxima of two peaks in (c). In (c), the color hue represents the phase difference between (a) and (b); the color hue is adjusted so that the redness denotes exactly $m=1$; the black isolines denote the amplitude $\sqrt{|\tilde{C}|}=7$ m/s; the horizontal error bar illustrates the temporal distribution of the USB- and LSB-like maxima indicated by the white crosses in Figures 2a-c, while the vertical bar illustrates the distribution of the estimated periods of RNM that can interact with SW2 and give rise to the maxima. (d,e,f) The same plots are (a,b,c) but from composite analyses between 2012 and 2017.

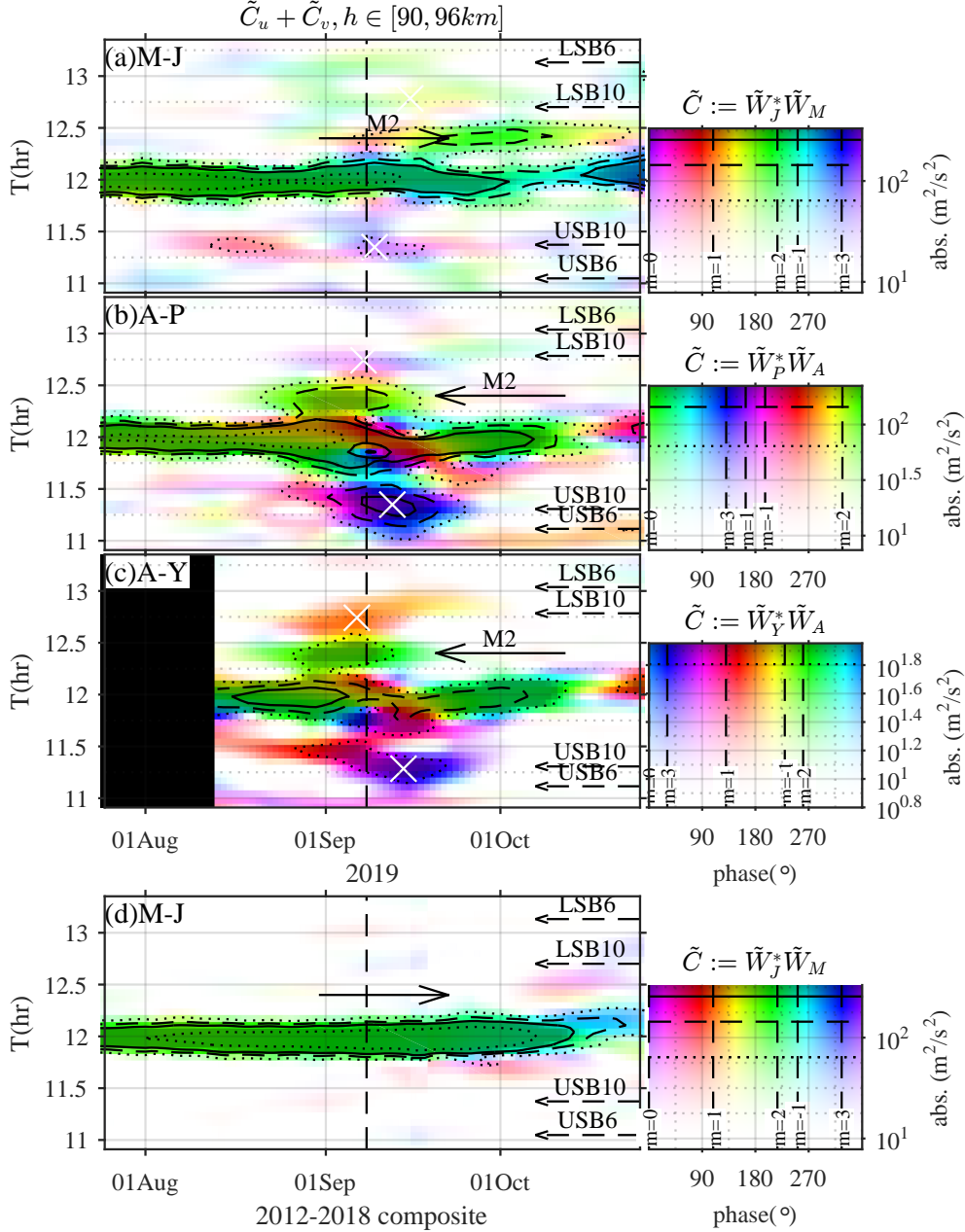


Figure 2: (a) Near-12hr CWL spectrum for the radar pair M-J, namely, similar plot as Figure 1c but summing the spectra of the zonal and meridional winds, averaged between 90 and 96km. All panels are adjusted so that blueness represents $m=3$. (b, c) Same plots as (a) but for the radar pairs A-P, and A-Y, respectively. (d) Same as (a) but for the 2012-2018 composite analysis. In each panel, the black isolines denote amplitudes at $\sqrt{|\tilde{C}|}=8, 12, 16$ and 24 m/s; the solid horizontal arrow indicates the M2-like signature; the dashed arrows on the most right-side illustrate the theoretical periods of the secondary waves (USB and LSB) of SW2-Q6DW and SW2-Q10DW nonlinear interactions; and the white crosses indicate local maxima of USB- and LSB-like peaks.

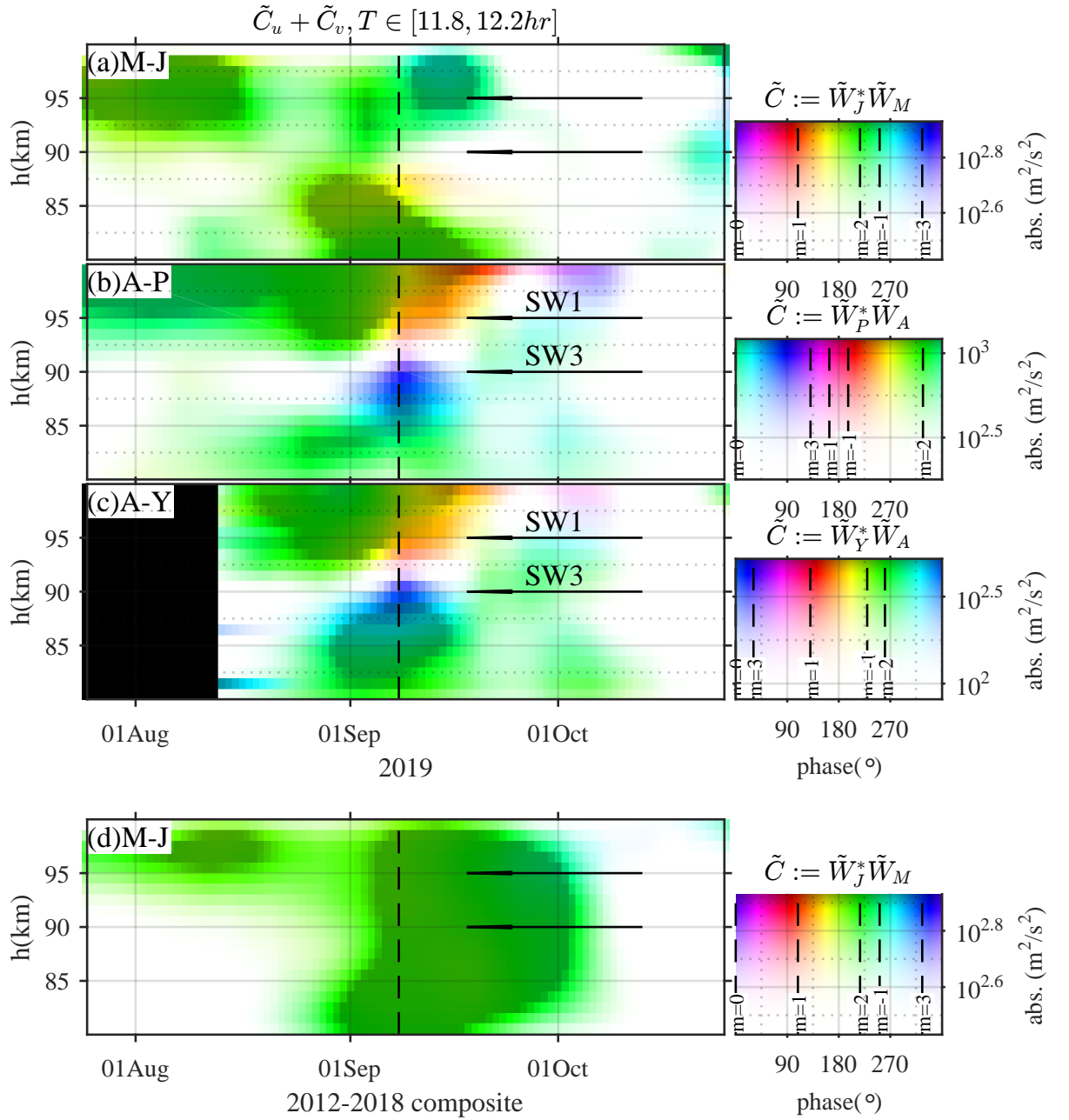


Figure 3: Same variable and panel arrangement as displayed in Figure 2 but as a function of date and altitude only at period $T=12.0hr$. For example, Panel (a) is combined from similar spectra as Figure 2a but at each individual altitude. The color is adapted so that green represents $m=2$. In (b,c), the horizontal arrows indicate SW1- and SW3-like signatures.

Net energy gain according to the Manley-Rowe relation

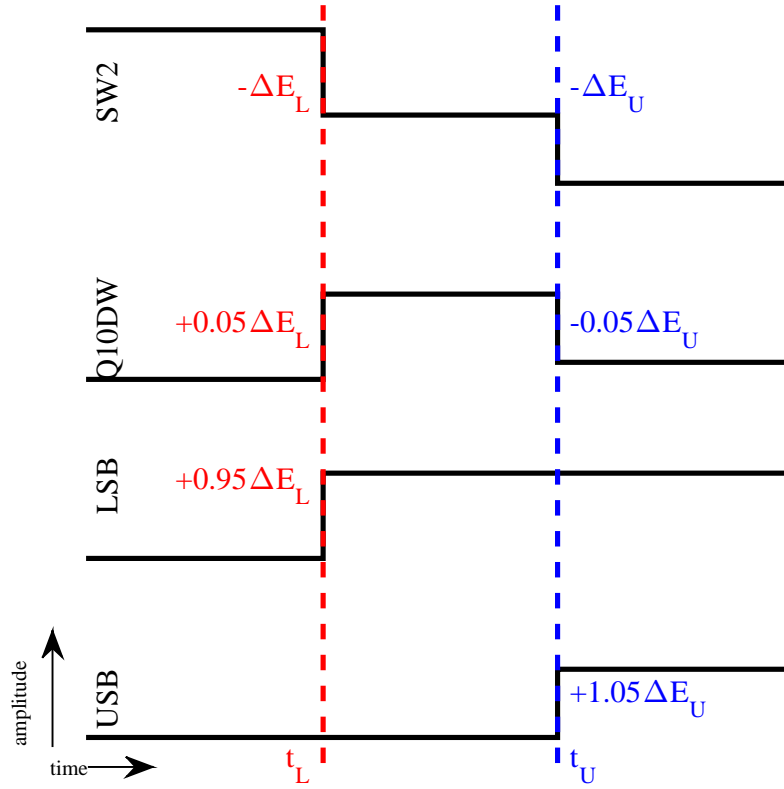


Figure 4: A sketch of net energy gain of the four waves in the Q10DW-SW2 nonlinear interactions according to the Manley-Rowe relation. The red and blue represent the LSB- and USB-generating interactions occurring at t_L and t_U , respectively. Between t_L and t_U maximizes the Q10DW. ΔE_L and ΔE_U are energy exchanged through SW2.

511 **Appendix A Aliasing between Q6DW and the secondary waves of Q6DW-**
 512 **SW2 nonlinear interaction**

513 Aliasing effects are intrinsic properties of all discrete signals. According to the Nyquist
 514 sampling theorem, a signal at frequency f_0 , with a sampling frequency f_s and Nyquist
 515 frequency $f_N := f_s/2$, is indistinguishable from signals at $f = (Zf_s + f_N) \pm |f_0 - f_N|$
 516 for all integers Z , and therefore they are aliases of each other. The largest near-zero dis-
 517 distinguishable frequency range is $[0, f_N)$. Readers are referred to Salby (1982) for a detailed
 518 description of the aliasing of the single-spacecraft approaches. Here, for a concise expla-
 519 nation, we consider a situation over the equator, where the temporal sampling interval
 520 of slowly precessing polar orbiter for a given longitude is about 12hr, or $f_s = 2\text{d}^{-1}$ and
 521 $f_N = 1\text{d}^{-1}$. A Q6DW signal at $f_0 = 0.2\text{cpd}$ is associated with aliases at $f = 1.8$ and
 522 2.2cpd , namely, the frequencies of the secondary waves of Q6DW-SW2 interactions. Note
 523 that this aliasing is independent from the coordinate systems. In the sun-synchronous
 524 coordinates system and for a given local time, f_s equals to the number of orbits per day
 525 (up to 15-16, e.g., in the case of Swarm) and f_N equals to 7.5-8cpd. However, the three
 526 waves are still indistinguishable because they are Doppler-shifted to the same frequency
 527 $|f| = 0.8\text{cpd}$. (A wave at f_0 in the earth-fixed frame is Doppler-shifted to $f_S = f_0 - m$ in
 528 sun-synchronous frames.)

Supporting Information for ”Quasi-10-day wave and semi-diurnal tide nonlinear interactions during the southern hemispheric SSW 2019 observed in the northern hemispheric mesosphere”

Maosheng He¹, Jorge L. Chau¹, Jeffrey M. Forbes², Denise Thorsen³,

Guozhu Li⁴, Tarique Adnan Siddiqui¹, Yosuke Yamazaki⁵, Wayne K.

Hocking⁶

¹Leibniz-Institute of Atmospheric Physics at the Rostock University, Kühlungsborn, Germany

²Ann & H.J. Smead Department of Aerospace Engineering Sciences, University of Colorado, Boulder, USA

³Department of Electrical and Computer Engineering, University of Alaska Fairbanks, Fairbanks, Alaska, USA

⁴Key Laboratory of Earth and Planetary Physics, Institute of Geology and Geophysics, Chinese Academy of Sciences, Beijing, China

⁵GFZ German Research Centre for Geosciences, Potsdam, Germany

⁶University of Western Ontario, 1151 Richmond St. London, Ontario, Canada N6A3K7

Contents of this file

1. Figures S1 to S2

Additional Supporting Information (Files uploaded separately)

Captions for Figures S1 to S2.

Introduction

This SI comprises two figures. Figure S1 illustrates the geographical distribution of the radars used in the current study. Figure S2 illustrates the existence of RWNs, Q10DW and Q6DW, at two latitudes.

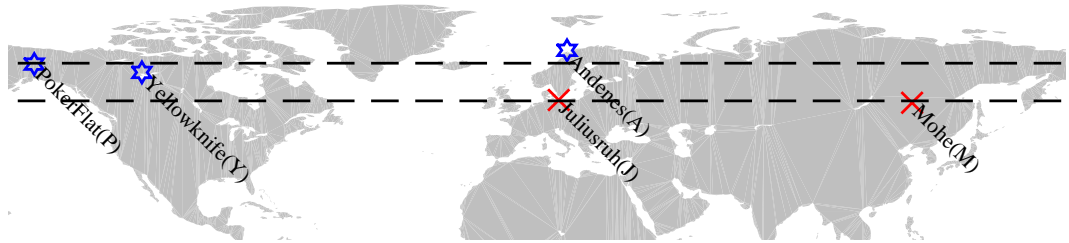


Figure S1. Distribution of the five meteor radars used for the current work. Two colors represent two latitude groups. Inside each groups, radars are paired to use the dual-station approach, PDT.

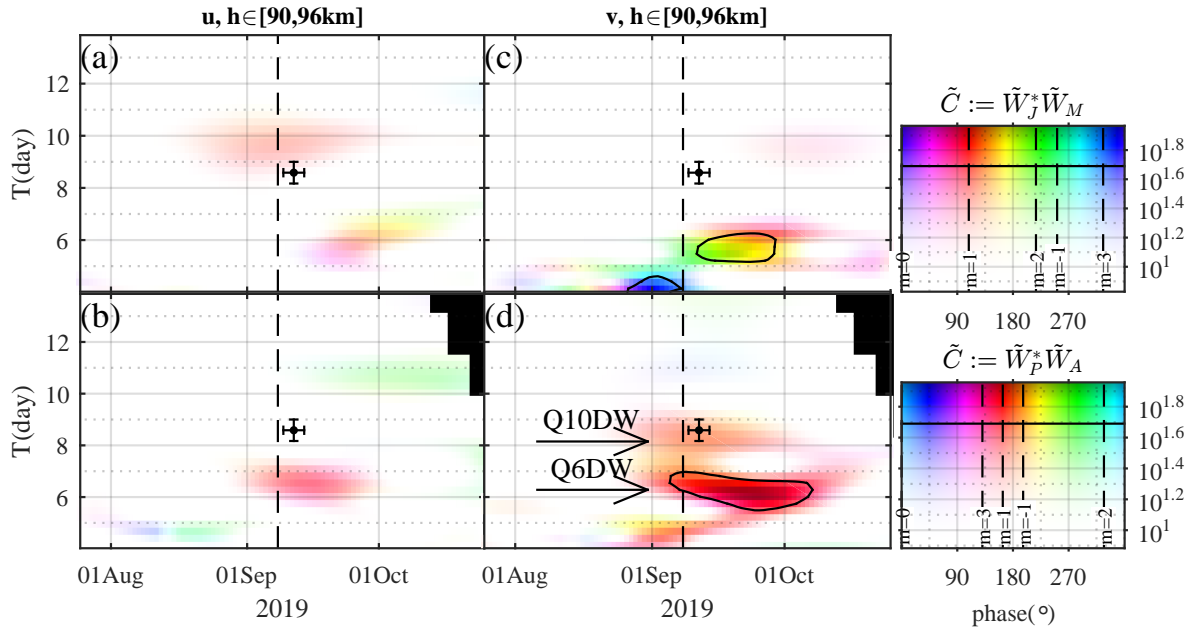


Figure S2. (a) CWL spectrum for the radar pair J-M, namely, same plot as Figure 1c but averaged between 90 and 96km. (b) Same plots as (a) but for the radar pair P-A. (c, d) Same plots as (a, b) but for meridional wind. In (d), the arrows indicated the maxima of the peaks at $T=8-9$ and $5-7$ d. To resolve these two peaks, the wavelet analysis, in all panels here, is carried at a higher frequency resolution than that in Figure 1. Consequently, the time resolution is lower here, and the peaks are smeared out in time domain.